High Cadence Imaging-Spectroscopy of Mercury's Exosphere

Carl Schmidt (1,2), Jeffrey Baumgardner (1), Luke Moore (1), Tom Bida (3), Ryan Swindle (4), Patrick Lierle (1)

(1) Boston University, Boston, MA, USA (schmidtc@bu.edu) (2) LATMOS, CNRS, Paris, FR (3) Lowell Observatory, Flagstaff, USA (4) Air Force Research Labs, Kihei, HI, USA

Abstract:

Ground-based observations of Mercury's exosphere are intrinsically difficult due to its proximity to the Sun. Observations must be made either in daylight or during brief windows at twilight. While the twilight background is far preferred, high airmass effects of Earth's atmosphere, windshake, and guiding all present formidable challenges towards spatially resolving the exosphere's structure. This study explores how such effects can be mitigated using results from a new instrument for high cadence spectroscopy, the Rapid Imaging Planetary Spectrograph (RIPS). While high cadence observations do not significantly improve upon the resolution floor imposed by atmospheric seeing, the method does mitigate obstacles such as telescope tracking inaccuracy, windshake, and flux calibration. Whereas daytime observing has been the predominant methodology in past exosphere studies, the twilight observations performed in this study easily resolve distinct brightness enhancements co-located with Mercury's magnetic cusps—regions that are diagnostics of charged particle precipitation and space weather effects. Structure in the sodium exosphere generally appears both more extended and brighter over the southern cusp, which has a broader open magnetic field line region. However, a northern enhancement during one observation confirms that the exosphere responds dynamically to environmental drivers, presumably changes in the solar wind dynamic pressure and/or interplanetary magnetic field.

1. Background:

Mercury's exosphere offers insight into the composition of its topmost surface, and the interaction of this surface with the local environment of interplanetary dust, neutral and charged particles and intense sunlight. Sodium is both the dominant atom in Mercury's exosphere and the dominant planetary ion in its magnetosphere (Killen et al. 2019; Raines et al. 2015). Conveniently, Na is also brightest spectroscopic emitter. While faint emissions of other species require off-disk observation, the several megaRayleigh Na D line emissions can be easily distinguished from the tens of MR/Å solar continuum that is scattered from the planet's dayside. Na emissions are therefore an important tool for understanding the interaction of Mercury's surface with its local environment.

Ground-based studies have largely reported that structure of the Na exosphere is episodic and enhanced at the poles (reviewed by McClintock et al. 2019; Killen et al. 2007). Early studies recognized polar enhancements as coupling between the exosphere and magnetosphere (Potter and Morgan 1990). It was later understood that such polar enhancements could also naturally track sources of locally-enhanced Na abundance in surface mineralogy, since MESSENGER orbiter Gamma Ray Spectrometer measurements have shown soil concentrations to increase at high latitudes, at least in the north (Peplowski et al. 2014). Still, the rapid morphology of polar exosphere spots on hourly or shorter timescales indicates a magnetospheric driver, such as ion sputtering (e.g., Leblanc et al. 2009; Orsini et al. 2018; Massetti et al. 2017), is more likely responsible.

Na emissions over the southern magnetic cusp are sometimes reported to be brighter than those in the north (Leblanc et al. 2008; Baumgardner et al. 2008; Mangano et al. 2013). This is perhaps a consequence of Mercury's offset magnetic dipole, which is predicted to channel four times more plasma precipitation to the southern surface than to the north (Anderson et al. 2011; Winslow et al. 2012). Also, the north-south asymmetry is typically inverted in the escaping neutral Na tail (Potter and Killen 2008), indicative of enhanced sources in the southern hemisphere (Schmidt 2013). Yet multi-year surveys show no statistical evidence that sodium emissions are on-average brighter in the south hemisphere than in the north (Potter et al. 2006; Mangano et al. 2015), and so the nature of polar enhancements remains unclear.

Ground-based evidence for magnetosphere-exosphere coupling seemingly contradicts the steady, seasonal repeatability of *in situ* Na data from MESSENGER UVVS. Cassidy et al. (2015, 2016) published 10 Mercury years of Na observations showing a persistent seasonal variation markedly absent of sporadic changes or high-latitude enhancements. The Na column peaked at aphelion, where its solar-driven sources are weakest. Moreover, this enhancement evidently tracks the cold-pole longitudes, two geographic longitudes that alternately face sub-solar at aphelion due to Mercury's 3:2 spin-orbit resonance. Two interpretations could plausibly explain such behavior. First, as a volatile, the sodium supply in the top-most soil could be quite sensitive to the maximum annual surface temperature. Na may have simply "baked-out" of the regolith grains, exhausting its supply in all but the coldest regions: high latitudes, and cold-pole longitudes where surface temperatures peak ~130K below their hot-pole counterparts. Though current knowledge of Na soil concentrations cannot inform this theory, the chemically-analogous potassium surface abundance supports this perspective (Peplowski et al. 2012). A second interpretation involves the bouncing and sticking of exospheric atoms over the surface. Cold-pole longitudes also locate at the terminators during perihelion. Solar driven support of the exosphere peaks at perihelion and could send Na atoms bouncing across the ~700K dayside until they stick to the first cold surface they encounter behind the terminator. Surrounding perihelion, Mercury revolves nearly as fast as it rotates, so the progression of local time nearly stands still and the solar sidereal motion even becomes slightly retrograde. The terminators remain at nearly fixed longitudes for 15% of Mercury's year surrounding perihelion, and so cold trapping here could locally enhance the reservoir of Na within the topmost regolith. Both scenarios could be causal to the cold-pole enhancements that UVVS observed in the Na exosphere, and models have not yet determined which of these two influences dominates.

Though the ground-based and MESSENGER-based results each paint significantly different portraits of the Na exosphere, both may be consistent knowing the limitations of each observer. From the spacecraft's elliptical orbit, operationally-constrained UVVS viewing geometry was ideal for exploring structure in local time, but its sight lines often integrated though latitudinal structure. Consequently, UVVS may have missed the most variable polar regions of the exosphere. Its limb-scan durations may have also exceeded characteristic timescales for variability, which could potentially be as short as ~10 min, the ballistic flight time associated with 1 km/s characteristic ejection energies of Na atoms from the surface. On the other hand, it is uncertain to what degree the variability and structure reported in multiple ground-based studies results from residual features that are introduced during the isolation and removal of artefacts in an intrinsically difficult observation. In any case, the low latitude variability reported in multiple ground-based studies (Potter et al. 1999; Kameda et al. 2007; Mangano et al. 2015, etc.) is in disparity with the seasonal UVVS results of Cassidy et al. (2015, 2016).

Challenges associated with observing Mercury through high airmass are so severe that solar telescopes, which suffer high daytime sky-background, are presently the primary tool for ground-based studies. Seeing and atmospheric transmission often change on minute timescales as the sight line encounters haze layers near the horizon. Consequently, flux calibration cannot use standard stars, with the exception of wide-field coronagraphs that record field stars concurrently (e.g., Schmidt et al. 2010). Photometric models of Mercury itself must therefore be employed. Setting aside potential model inaccuracies (Domingue et al., 1997), such calibration must either integrate the entire disk emission, or in cases where only a portion of the disk is observed, have a metric for the instantaneous seeing that subtends a sizable fraction of the planetary disk. Windshake can further exacerbate blurring on several second timescales. Slower pointing drift is often problematic as well since pointing models can prove inaccurate at low altitudes due to telescope flexure, and closed-loop guiding may not be possible on such a bright, non-radially symmetric, extended target. Differential atmospheric refraction also complicates pointing, since the guider and spectrograph must operate at similar wavelengths to refract equally within arcsecond scale length tolerances. Guide cameras on most spectrographs function independently from the spectral detector, introducing ambiguity when cross-referencing their exposures as a result of the aforementioned issues.

To combat these challenges, the observational study herein explores a new technique for measuring the exosphere above Mercury's bright disk. Section 2 provides a description of the instrument. Observations made during three observing runs in 2018 are described in Section 3, and their analyses are reviewed in Section 4. Section 5 offers interpretation of these results.

2. RIPS Instrument Design:

The Rapid Imaging Planetary Spectrograph (RIPS) was designed to measure a long-slit high-resolution spectrum and monochromatic image concurrently on the same detector, so that spectroscopy is paired with an unambiguous reference for pointing, blurring effects and relative flux. An Andor iXon 1024 x 1024 EMCCD records both an image and a spectrum at fast frame rates up to 30 fps. Four motors in RIPS control echelle grating angle, slit-width, and focus settings for both spectral and imaging channels. Typical Mercury observations would have the slit-aligned with the planet's spin axis. To set the position angle of the slit accordingly, the entire instrument rotates about the optical axis using an additional motor and gear mesh.

The optical path exiting the telescope first encounters an ~18Å FWHM pre-filter, which minimizes off-band light from entering the instrument and being scattered within. The telescope's exit pupil lies at the spectrograph slit plane. After reflection off the slit jaws, one light path is guided into the imaging channel on the lower half of the CCD and passes through two filters: a 0.1 transmission neutral density filter, used to better match the dynamic range of the imaging channel to that of the spectral channel, and a narrowband (4Å equivalent width) filter centered on the Na D_2 line used to couple the imaging and spectral channels to the same differential atmospheric refraction.

Light passing through the slit aperture continues to a flat folding mirror, which re-directs the diverging beam into a collimating lens. Once dispersed by an echelle grating, the beam passes back through this collimating lens (now acting as an objective lens), back to the folding mirror, to another mirror which re-directs to a field lens where the first image of the spectrum is formed. In this arrangement, the echelle grating is operating within only ~1.5° of Littrow. It yields a 24.6

mÅ/pixel dispersion at sodium wavelengths corresponding to 1.25 km/s/pixel. Echelle orders are isolated using a ~60Å sorting filter. Spectral resolving powers of up to R=97,000, a 2.45 pixel FWHM, are achieved with the narrowest ~20µm slit width. Although the pre-filter is, in principle, redundant with the Na filters in both instrument channels, internal reflections permit ample stray light to warrant its implementation despite the anti-reflection coated optics.

3. Observations:

Three observational campaigns were completed during 2018 solar elongations, one at the 1.8m Perkins telescope (Anderson Mesa, Arizona) and two at the 3.7m Advanced Electro Optical System (AEOS) telescope (Haleakalā, Hawaii). Table 1 lists the data acquired. On each date, the observing sequence split the available time in order to target both sodium and potassium emissions. Only the sodium EMCCD mode observations are presented here. During the first light observations in Arizona, the telescope pointing was offset only once, since Earth's atmosphere, windshake and pointing drifts otherwise provided the 4" motion needed for the slit to fully sample the planetary disk. AEOS on the other hand, locked onto a fixed image of the disk using adaptive optics, requiring the slit aperture to be manually scanned across the planetary disk. To achieve this, RIPS was pivoted on a stage, except for on June 23rd when we employed drift scans without tracking or adaptive optics.

Table 1: 2018 Observations of alkalis with RIPS.

UT Start (2018)	Airmass	N_{frames}	Integration (s)	Filter	Mode	Notes
03-15 1:47:06-1:54:08	3.90-4.30	17 x 100	0.05	Na	EMCCD	
03-15 1:55:51-1:58:29	4.41-4.59	11 x 100	0.05	K	EMCCD	
06-21 5:33:03-5:39:10	5.52-6.28	2 x 500	0.5 / 1.0	Na	EMCCD	
06-21 5:48:58-5:53:58	7.99-9.25	2	200	Na	Conventional	Anti-Sunward
06-22 5:31:35-5:42:30	5.37-6.78	7	100	K	Conventional	
06-22 5:45:25-5:55:50	7.46-9.81	3	300	K	Conventional	Anti-Sunward
06-23 5:33:30-5:40:24	4.90-5.58	5 x 100	1	K	EMCCD	Drift Scan
06-23 5:48:18-6:00:36	6.61-9.21	7 x 100	1	Na	EMCCD	Drift Scan
06-24 5:46:56-5:50:48	5.99-6.53	2	200	K	Conventional	
06-24 5:55:06-5:58:37	7.24-7.95	2	200	Na	Conventional	
06-24 6:03:48-6:07:16	9.25-10.37	2	200	K	Conventional	
06-26 5:54:11-5:57:50	6.24-6.79	3 x 100	1	K	EMCCD	
06-26 6:02:00-6:11:02	7.55-9.86	6 x 100	1	Na	EMCCD	
12-12 15:36:14- 15:47:11	12.80-8.69	7 x 100	1	Na	EMCCD	
12-12 15:51:11- 16:25:29	7.75-4.00	5 x 100	5	K	EMCCD	
12-13 15:38:51-15:49:23	11.46-8.11	7 x 100	1	Na	EMCCD	
12-13 15:54:06-16:02:29	7.15-5.91	2 x 100	5	K	EMCCD	
12-13 16:12:07-16:20:45	4.91-4.28	5	100	K	Conventional	
12-13 16:22:49-16:29:59	4.15-3.76	3	200	K	Conventional	

An example RIPS frame is seen in Figure 1. Its spectral range spans only 25Å. With 12% magnification, the spectral channel is a highly dispersed mirrored image of the light that passed through the slit aperture in the imaging channel. The imaging channel plate scale well-samples the point spread function at 0.106″/pixel at Perkins and 0.045″/pixel at AEOS. Mercury's exospheric emission can be seen blue-shifted from the solar absorption owing to its heliocentric velocity.
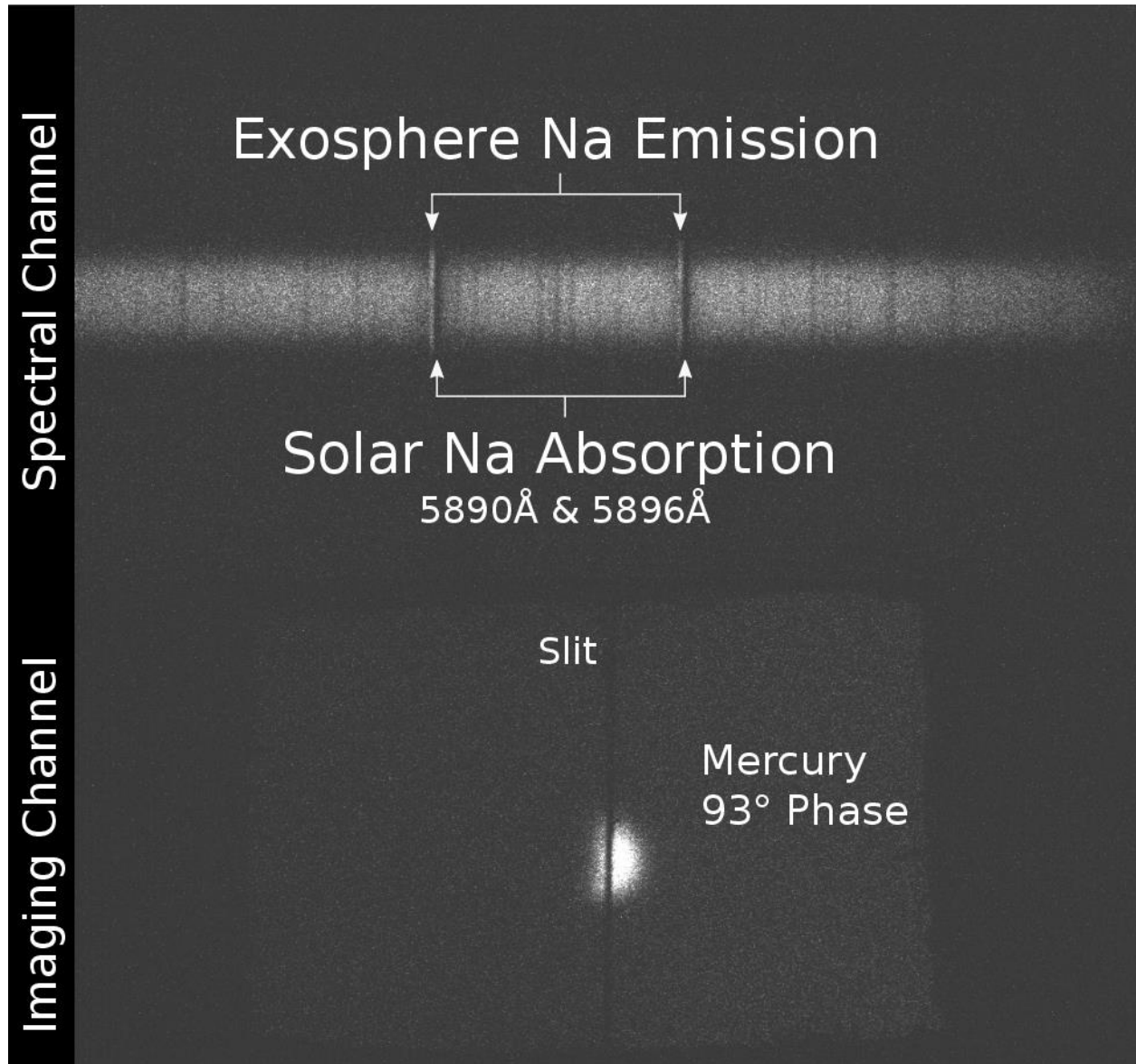
Figure 1: Example of a raw 0.05s frame from first light at the Perkins 1.8m telescope. 1700 such frames were taken over 7 min, sufficient to characterize the exosphere during the brief observing window at twilight.

4. Photometric Modeling and Analysis:

A photometric model of Mercury's surface reflectance is central to the RIPS data analysis. The formulation of Hapke (2012; Eqn. 12.55) is applied using parameters that Domingue et al. (2016) fit to the MESSENGER Mercury Dual Imaging System (MDIS) dataset. Basic Hapke parameters are interpolated from the MDIS filter wavelengths to 5893Å. Reflectivity is calculated for the instantaneous observing geometry, using the instrumental plate scale and Mercury's angular size to determine the bi-directional reflectance at each pixel. The product of this reflectance and

the solar spectral irradiance[1] given Mercury's instantaneous heliocentric range and velocity then determine the disk's theoretical brightness at a given pixel and wavelength. For convenience, this photometric model is rotated into plane-of-sky coordinates (celestial north as vertical, west as horizontal).

Standard bias and flat corrections are made to both RIPS channels. Files are normalized for exposure time and the imaging and spectral channels are each written to data cubes for independent processing. The imaging channel is transposed and rotationally aligned into plane-of-sky coordinates. The sole observation from the Perkins telescope was taken with two different slit position angles, and AEOS, as an az-alt telescope, delivered an image that rotated during the course of the observations. After bilinear interpolation across the slit, rotational alignment is determined by cross-correlating the imaging channel with the photometric model blurred by an initial seeing estimate. After rotational alignment, frames are then translationally co-aligned to the blurred photometric model. Since co-alignment about the Mercury-Sun axis depends on atmospheric seeing, this alignment routine also blurs the model with a range of seeing conditions using Gaussian convolution kernels. When the correlation matrix between the imaging channel and blurred photometric model is maximized, a downhill simplex algorithm returns estimates of both the instantaneous effective seeing and the cardinal direction alignment for each frame.

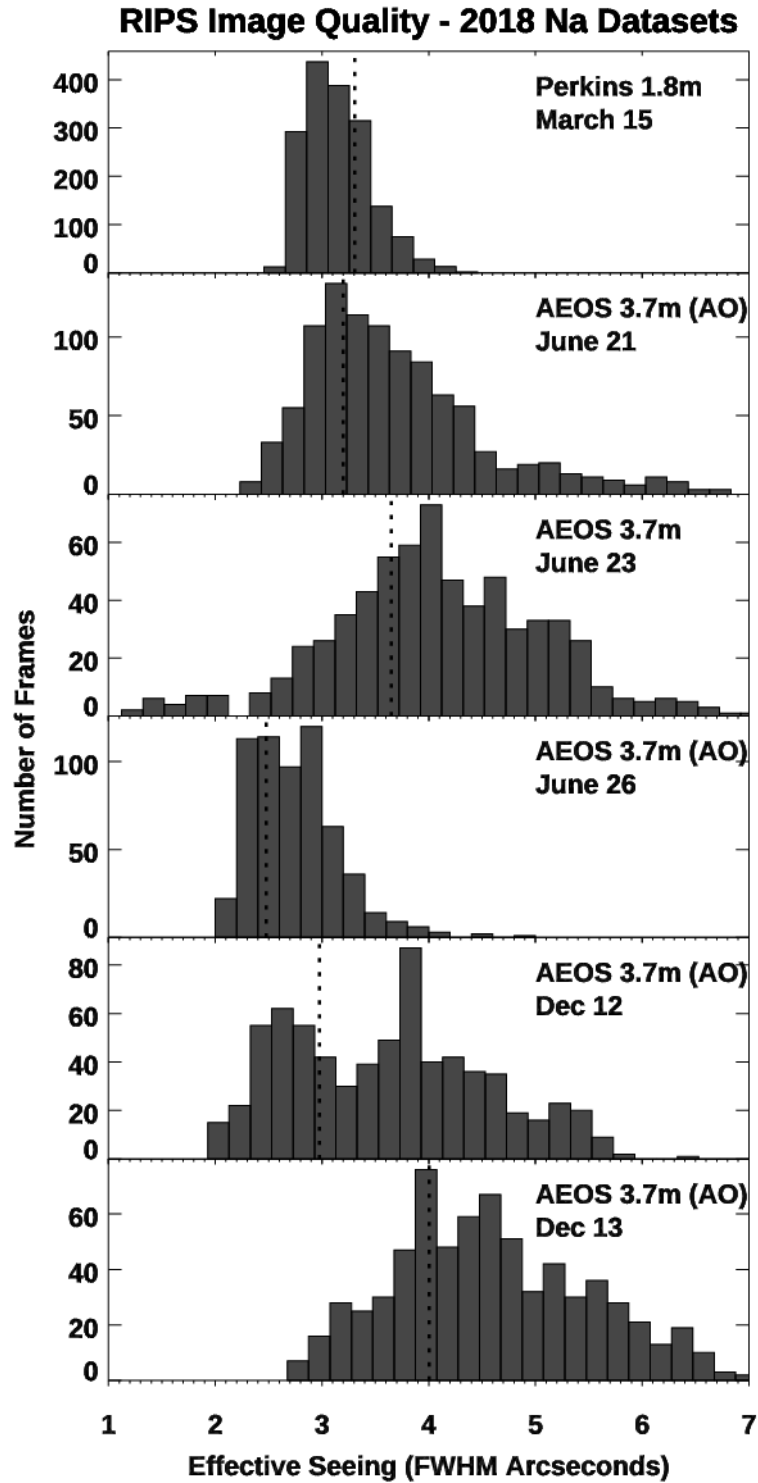[1] See http://kurucz.harvard.edu/sun/irradiance2005/

Figure 2. Empirical PSF widths for the RIPS imaging channel EMCCD measurements of the Na exosphere. Both conventional and adaptive optics configurations are shown. Dotted lines represent accept-reject thresholds used throughout this study. For airmass, see Table 1.

Rotational and translational alignments determined from the imaging channel are applied to the 1-dimensional spectral channel, filling in a monochromatic image using the planet's motion relative to the slit aperture. To extract the sodium signal in each frame, a solar spectrum is matched in resolution and fit to the observed continuum at each spatial pixel. The residual is summed over linewidth. This 1-dimensional total of the exospheric counts must then be spread over the 2-D region subtended by the slit's width. This is done using weights from a normal probability distribution, which well-represents the line spread function since the slit is unresolved. Frames are combined as the weighted arithmetic mean of a stack of exposures, and frames with effective seeing below a specified threshold are zero-weighted.

Effective seeing, that is, seeing convolved with instrumental point spread function, is applied as a metric for acceptance/rejection of individual frames. The concept here is that occasional frames could, for a fraction of a second, capture images through minimal atmospheric turbulence and begin to approach a diffraction-limited image quality (e.g., Fried 1978). Figure 2 compares effective seeing with and without adaptive optics. Histograms based on measured blurring in the imaging channel show, perhaps unsurprisingly, that turbulence levels during first light at the Perkins 1.8m were largely homogeneous in the 3.9-4.3 airmass range. Subsequent nights at the AEOS 3.7m demonstrate that it was also challenging for adaptive optics to correct wavefront distortions during those observing conditions. With adaptive optics an often improved, but much broader range of effective seeing values were measured, largely due to conditions of atmospheric haze and the still higher airmass.

Flux calibration is performed by summing over a 1Å region of continuum and processing it alongside the integrated brightness of the combined Na D_1 and D_2 exosphere lines. The sensitivity in Rayleighs / DN / s is taken to be the brightness of the photometric model divided by the recorded continuum. Multiplying this sensitivity by the exosphere maps reconstructed from the spectral channel then flux-calibrates the data. Since both the continuum and photometric model are spatially integrated over the entire disk, this calibration is independent of the effective seeing, at least at the global level. Most importantly, the continuum images are an identically matched reference for the spatial reconstruction of the exosphere images, leaving no ambiguity about the quality of the spatial information obtained or processing artefacts from improper alignment. The absolute flux of the exosphere can finally be reduced to column density using standard calculations of the sodium excitation rate by solar photons.

5. Results:
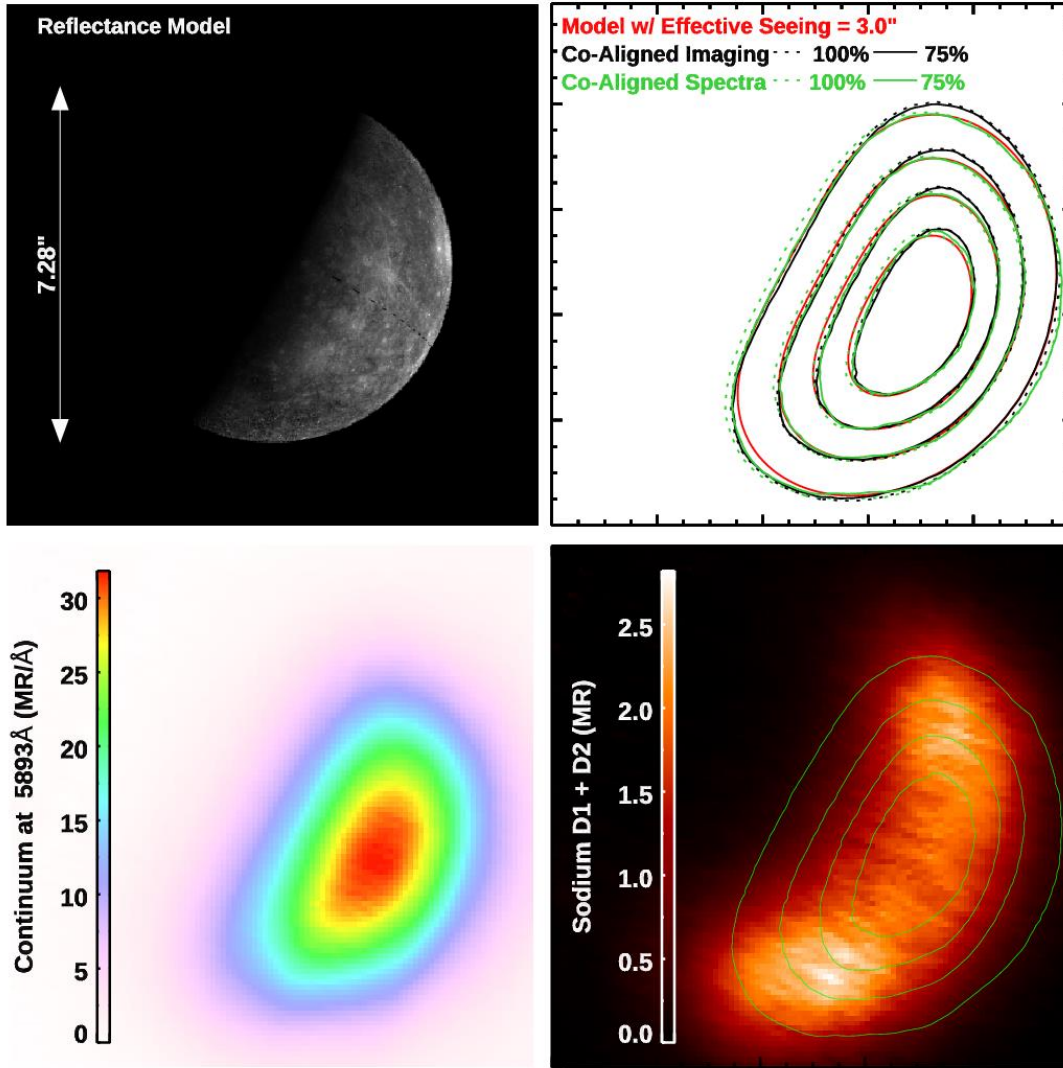
RIPS --- 2018-03-15 01:47 --- True Anomaly 28.8°

Figure 3. First light RIPS observations at the 1.8m Perkins telescope in Arizona.

Figure 3 shows results from processing the instrument's first light observations. The photometric model with a MESSENGER MDIS mosaic overlay is shown in the top left panel. The top right panel shows contours of the photometric model blurred by 3″, that is, the mean effective seeing within the sharpest 75% of images per Figure 2. The contours indicate a noticeable, but only marginal improvement via downselecting the best 75%. At 20% intervals, the dotted and solid contours nearly overlap, delineating the 75% best and "no rejection" cases. The continuum image reconstructed from 1Å of signal in the spectral channel is shown at bottom left, and as green contours in the right panels. Na emission levels of 3 MR for both D lines are broadly consistent with prior disk-averaged datasets at this season (e.g., Leblanc and Johnson 2010). Enhancement over both poles is evident. The southern polar region is both brighter and more extended than the

north. A relative deficiency of sodium at low latitudes is evidenced by comparing emissions to reflected continuum contours in the bottom right panel. Near the dawn terminator, this results partly from a face-on viewing as opposed to a higher slant column through the exosphere. Still, the exosphere's subsolar content is markedly absent, particularly considering Mercury is less than five days post perihelion.
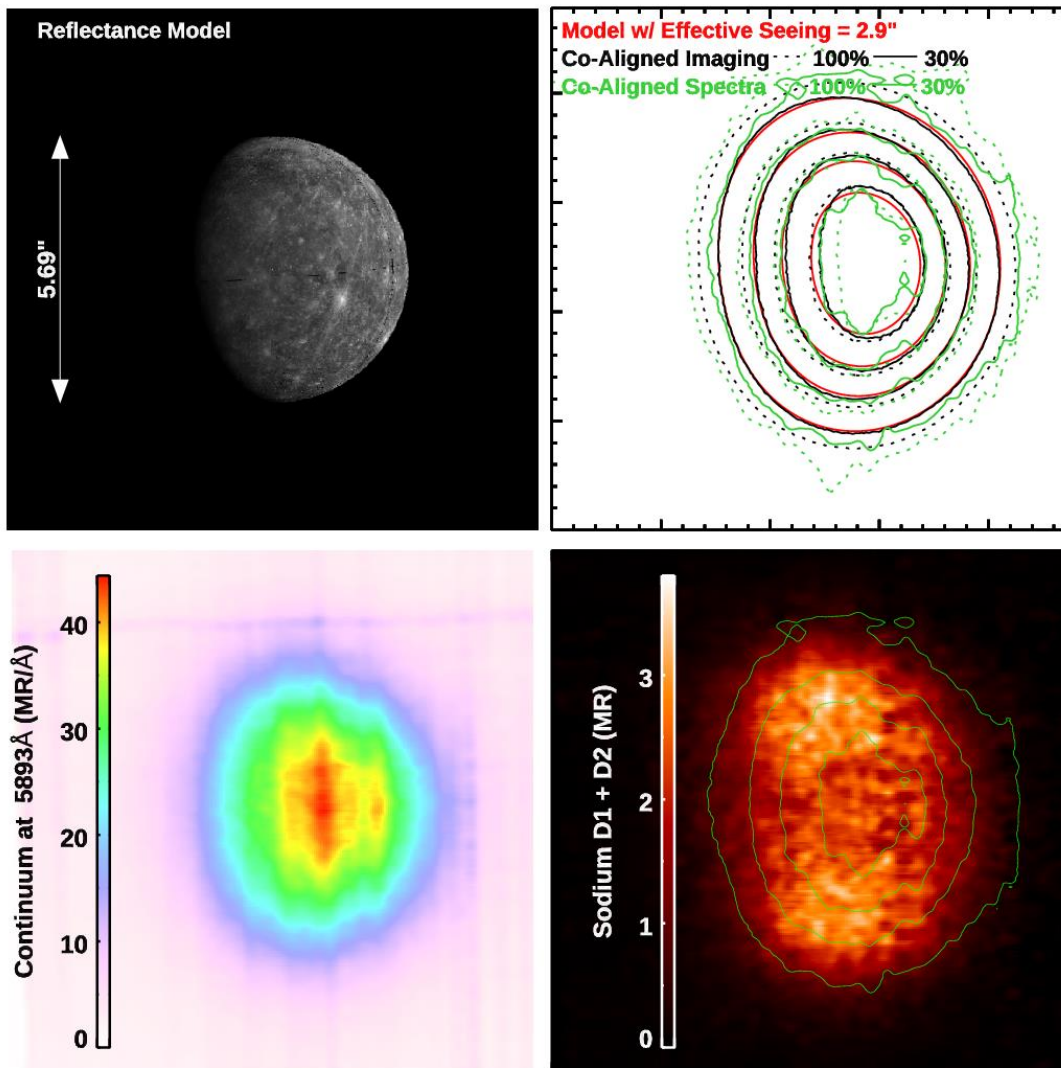
Figure 4. Observations from the AEOS telescope in Haleakalā, showing a brighter northern enhancement in the exosphere's emission.

Lower image quality in Figure 4 is seen relative to Figure 3. Although a similar mean effective seeing is contained within a 30% threshold, fewer frames are accepted. Additionally, the 22% smaller apparent size of Mercury is more susceptible to blurring and the 2.35x magnified plate scale at AEOS requires more steps for the slit aperture to scan the disk. Combined with the fewer samplings per unit area of the disk, effective seeing variations as the slit is scanned produce

more jagged contours in the spatial reconstructions derived from the spectral channel. Polar enhancements are still recognizable. The June 21st measurements uniquely show a brightness peak in the northern region. Better image quality in Fig. 5 shows the southern enhancement was restored within a few days, at which time the 0.7 north/south ratio was the most significant asymmetry that RIPS recorded. Polar enhancements also appeared when viewing the planet's evening hemisphere. Fig. 6 shows dusk-side structure that is similar to the dawn-side in Figure 3. Observations June 23 and Dec 13 also yielded similar structure to Figures 5 and 6, but with lower spatial resolution.
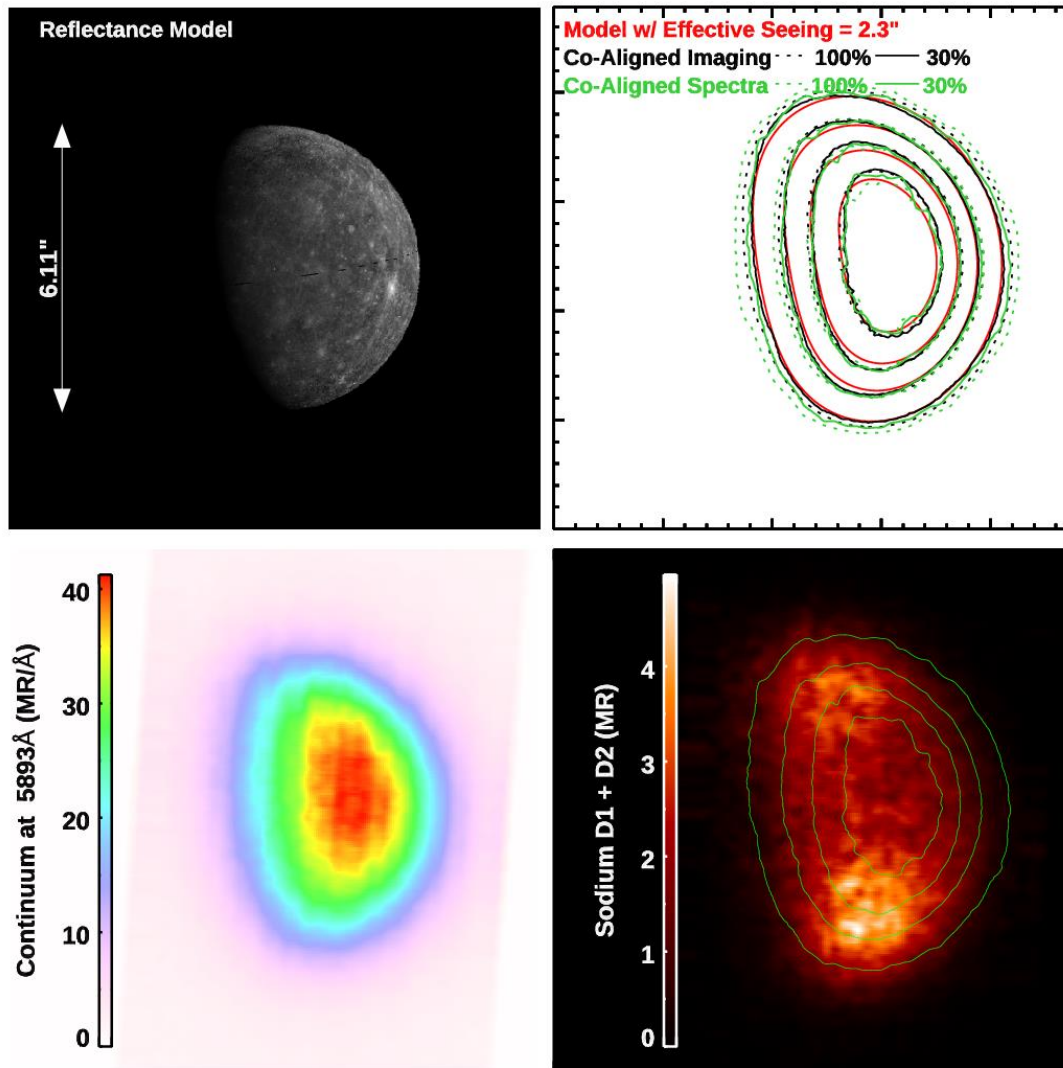

Figure 5. Same as Fig. 4, exhibiting a brighter southern enhancement several days later.
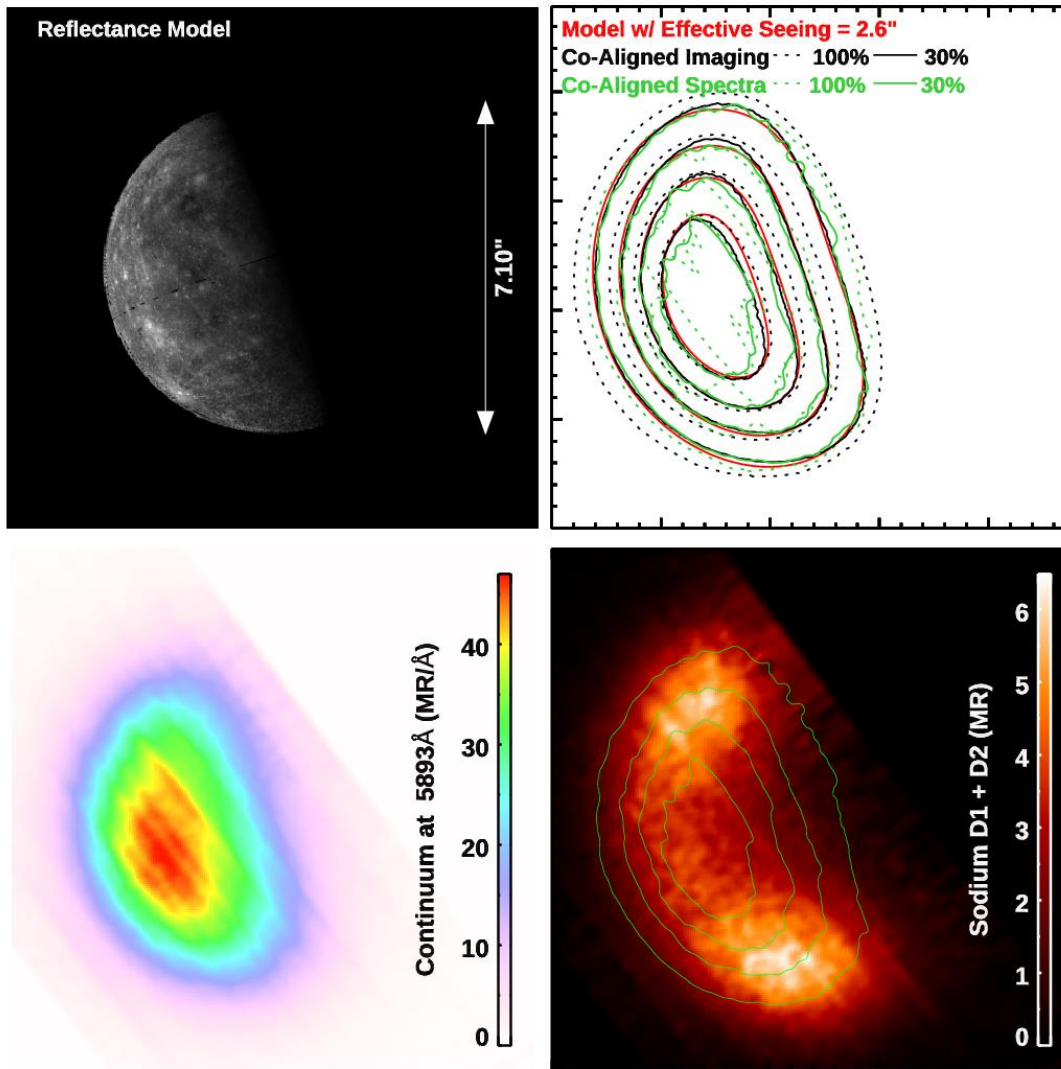
RIPS --- 2018-12-12 15:36 --- True Anomaly 76.5°

Figure 6. Same as Figures 4 and 5, but with viewing geometry facing the planet's evening hemisphere.

6. Interpretation and Deconvolution:

All of the reconstructed exosphere maps show brightest emissions near the poles rather than low latitudes. This context is important for comparisons with UVVS orbital data, which made limb scans with minimum tangent altitudes almost exclusively within the 45°S to 35°N latitude range (see Cassidy et al. 2015, Fig. 3). Five of the six measurements that RIPS made in 2018 show an enhancement in the south polar region, as anticipated for sourcing coupled to plasma precipitation. Yet, the north/south emission ratio is far less pronounced than ion-sputtering would forecast. A factor of ~1.4 southern enhancement over the north is the greatest that RIPS observed,

while southern cusp precipitation is predicted to occur over 4 times the surface area (Winslow et al. 2012). As in past AEOS measurements using a fiber-fed instrument (Baumgardner et al., 2008), the median enhancement is close to 1.2 south-to-north. If one presumes the latitudinal dependency of Na soil abundance in the southern hemisphere mimics that which MESSENGER GRS observed in the north (Peplowski et al. 2014), then the 11° difference in cusp latitude cannot account for such a small 1.2 asymmetry factor.

Characteristic size scales of the exosphere's structure are unresolved here. Reducing the emission maps to column density using their photon excitation rates would in turn underestimate the Na content at the brightest polar regions. In theory, however, more accurate column estimates can be obtained with further processing. In cases of good image quality, the photometric model blurred with a Gaussian convolution kernel can effectively forward model the continuum contours reconstructed from the spectral channel. Perhaps then deconvolution of this same kernel could be applied to attain higher spatial resolution.
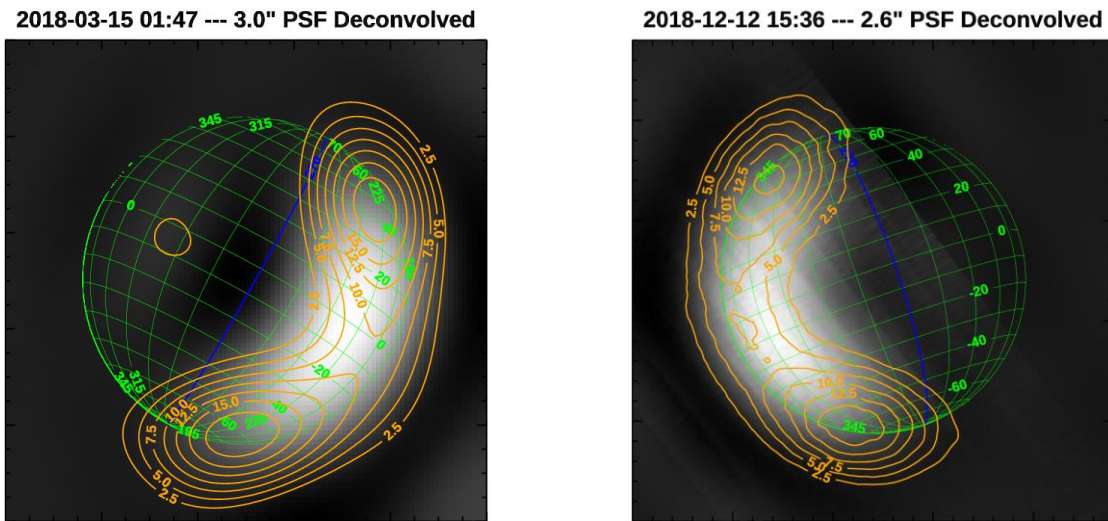

Figure 7. Maximum Likelihood deconvolution of the continuum and Na exosphere maps in Figures 3 and 6. Gray shading represents continuum surface reflectance. Contours give the Na column density in 10^{10} cm^{-2} units. The cold-pole longitudes, marked in blue co-locate near the terminator.

Figure. 7 shows the result after 100 iterations of a Maximum Likelihood deconvolution algorithm (Varosi and Landsman 1993). Again, the continuum image is processed identically alongside the exosphere, which is shown as contours representing Na column density in units of 10^{10} cm^{-2}. This technique produces artefacts, limiting its usefulness, but some conclusions may still be drawn. There is a paucity of any significant density at cold-pole longitudes that cannot be attributed solely to viewing geometry. This may indicate the feature only becomes prominent farther from the dawn-dusk terminators, between mid-morning or mid-afternoon. Based on Fig. 7, the peak column at both polar spots is 2 x 10^{11} cm^{-2} on March 15, and slightly lower on Dec 12, perhaps since Mercury is farther from the Sun. Blurring remains an issue so the local column could be denser and this should be considered a lower limit. Blurring also shifts the apparent spot

locations inward towards the planet. Their true distribution almost certainly peaks tangent to the limb and not above the disk. The exosphere's spots are predicted to be offset northward due to the offset magnetic dipole, yet no such shift is observed here. Surprisingly, both observations show the northern enhancement falls equatorward of the southern enhancement. The spots are also equatorward of the expectation for magnetic cusps, which Winslow et al. (2012) suggest typically occur near 75°N and 64°S. The origin of this structure therefore remains somewhat enigmatic, both in terms of brightness and location. A larger dataset may yield insight, particularly if the brightness asymmetry exhibits any latitudinal dependence.

7. Conclusions:

High cadence techniques can overcome many of the difficulties associated with twilight observations of Mercury's exosphere at high airmass, and offer a viable alternative to daytime observations. The exosphere exhibits clear enhancements of comparable brightness at high latitudes and mid-day local times. These polar enhancements are variable on shorter timescales than the seasonal changes that MESSENGER has characterized at lower latitudes. On average, the exosphere's southern hemisphere is indeed brighter than the north, however not nearly to the extent predicted by plasma precipitation through the planet's offset magnetosphere.

References:

Anderson, Brian J., Catherine L. Johnson, Haje Korth, Michael E. Purucker, Reka M. Winslow, James A. Slavin, Sean C. Solomon, Ralph L. McNutt, Jim M. Raines, and Thomas H. Zurbuchen. 2011. "The Global Magnetic Field of Mercury from MESSENGER Orbital Observations." *Science*. https://doi.org/10.1126/science.1211001.

Baumgardner, Jeffrey, Jody Wilson, and Michael Mendillo. 2008. "Imaging the Sources and Full Extent of the Sodium Tail of the Planet Mercury." *Geophysical Research Letters*. https://doi.org/10.1029/2007GL032337.

Cassidy, Timothy A., William E. McClintock, Rosemary M. Killen, Menelaos Sarantos, Aimee W. Merkel, Ronald J. Vervack, and Matthew H. Burger. 2016. "A Cold-Pole Enhancement in Mercury's Sodium Exosphere." *Geophysical Research Letters*. https://doi.org/10.1002/2016GL071071.

Cassidy, Timothy A., Aimee W. Merkel, Matthew H. Burger, Menelaos Sarantos, Rosemary M. Killen, William E. McClintock, and Ronald J. Vervack. 2015. "Mercury's Seasonal Sodium Exosphere: MESSENGER Orbital Observations." *Icarus*. https://doi.org/10.1016/j.icarus.2014.10.037.

Domingue, Deborah L., Brett W. Denevi, Scott L. Murchie, and Christopher D. Hash. 2016. "Application of Multiple Photometric Models to Disk-Resolved Measurements of Mercury's Surface: Insights into Mercury's Regolith Characteristics." *Icarus*. https://doi.org/10.1016/j.icarus.2015.11.040.

Domingue, Deborah L., Ann L. Sprague, and Donald M. Hunten. 1997. "Dependence of Mercurian Atmospheric Column Abundance Estimations on Surface-Reflectance Modeling." *Icarus* 128 (1): 75–82. https://doi.org/10.1006/icar.1997.5725.

Fried, David L. 1978. "Probability of Getting a Lucky Short-Exposure Image through Turbulence*." *Journal of the Optical Society of America* 68 (12): 1651. https://doi.org/10.1364/JOSA.68.001651.

Kameda, S., I. Yoshikawa, J. Ono, and H. Nozawa. 2007. "Time Variation in Exospheric Sodium Density on Mercury." *Planetary and Space Science* 55 (11): 1509–17. https://doi.org/10.1016/j.pss.2006.10.010.

Killen, Rosemary, Gabrielle Cremonese, Helmut Lammer, Stefano Orsini, Andrew E. Potter, Ann L. Sprague, Peter Wurz, et al. 2007. "Processes That Promote and Deplete the Exosphere of Mercury." In *Space Science Reviews*. https://doi.org/10.1007/s11214-007-9232-0.

Leblanc, F., A. Doressoundiram, N. Schneider, S. Massetti, M. Wedlund, A. López Ariste, C. Barbieri, V. Mangano, and G. Cremonese. 2009. "Short-Term Variations of Mercury's Na Exosphere Observed with Very High Spectral Resolution." *Geophysical Research Letters* 36 (7). https://doi.org/10.1029/2009GL038089.

Leblanc, F., and R. E. Johnson. 2010. "Mercury Exosphere I. Global Circulation Model of Its Sodium Component." *Icarus*. https://doi.org/10.1016/j.icarus.2010.04.020.

Leblanc, Francois, Alain Doressoundiram, Nick Schneider, Valeria Mangano, A. López Ariste, C. Lemen, B. Gelly, Cesare Barbieri, and G. Cremonese. 2008. "High Latitude Peaks in Mercury's Sodium Exosphere: Spectral Signature Using THEMIS Solar Telescope." *Geophysical Research Letters* 35 (18). https://doi.org/10.1029/2008GL035322.

Mangano, Valeria, Stefano Massetti, Anna Milillo, Christina Plainaki, Stefano Orsini, Rosanna Rispoli, and Francois Leblanc. 2015. "THEMIS Na Exosphere Observations of Mercury and Their Correlation with In-Situ Magnetic Field Measurements by MESSENGER." *Planetary and Space Science* 115 (September): 102–9. https://doi.org/10.1016/j.pss.2015.04.001.

Massetti, S., V. Mangano, A. Milillo, A. Mura, S. Orsini, and C. Plainaki. 2017. "Short-Term Observations of Double-Peaked Na Emission from Mercury's Exosphere." *Geophysical Research Letters*. https://doi.org/10.1002/2017GL073090.

Orsini, Stefano, Valeria Mangano, Anna Milillo, Christina Plainaki, Alessandro Mura, Jim M. Raines, Elisabetta De Angelis, Rosanna Rispoli, Francesco Lazzarotto, and Alessandro Aronica. 2018. "Mercury Sodium Exospheric Emission as a Proxy for Solar Perturbations Transit." *Scientific Reports* 8 (1). https://doi.org/10.1038/s41598-018-19163-x.

Peplowski, Patrick N., Larry G. Evans, Karen R. Stockstill-Cahill, David J. Lawrence, John O.

Goldsten, Timothy J. McCoy, Larry R. Nittler, et al. 2014. "Enhanced Sodium Abundance in Mercury's North Polar Region Revealed by the MESSENGER Gamma-Ray Spectrometer." *Icarus*. https://doi.org/10.1016/j.icarus.2013.09.007.

Peplowski, Patrick N., David J. Lawrence, Edgar A. Rhodes, Ann L. Sprague, Timothy J. McCoy, Brett W. Denevi, Larry G. Evans, et al. 2012. "Variations in the Abundances of Potassium and Thorium on the Surface of Mercury: Results from the MESSENGER Gamma-Ray Spectrometer." *Journal of Geophysical Research E: Planets* 117 (10). https://doi.org/10.1029/2012JE004141.

Potter, A. E., and R. M. Killen. 2008. "Observations of the Sodium Tail of Mercury." *Icarus*. https://doi.org/10.1016/j.icarus.2007.09.023.

Potter, A. E., R. M. Killen, and T. H. Morgan. 1999. "Rapid Changes in the Sodium Exosphere of Mercury." *Planetary and Space Science* 47 (12): 1441–48. https://doi.org/10.1016/S0032-0633(99)00070-7.

Potter, A. E., R. M. Killen, and M. Sarantos. 2006. "Spatial Distribution of Sodium on Mercury." *Icarus* 181 (1): 1–12. https://doi.org/10.1016/j.icarus.2005.10.026.

Potter, A. E., and T. H. Morgan. 1990. "Evidence for Magnetospheric Effects on the Sodium Atmosphere of Mercury." *Science* 248 (4957): 835–38. https://doi.org/10.1126/science.248.4957.835.

Schmidt, C.A., J.K. Wilson, J. Baumgardner, and M. Mendillo. 2010. "Orbital Effects on Mercury's Escaping Sodium Exosphere." *Icarus* 207 (1). https://doi.org/10.1016/j.icarus.2009.10.017.

Schmidt, Carl A. 2013. "Monte Carlo Modeling of North-South Asymmetries in Mercury's Sodium Exosphere." *Journal of Geophysical Research: Space Physics*. https://doi.org/10.1002/jgra.50396.

Varosi, F., and W. B. Landsman. 1993. "An IDL Based Image Deconvolution Software Package." *Astronomical Data Analysis Software and Systems II* 52 (January): 515.

Winslow, Reka M., Catherine L. Johnson, Brian J. Anderson, Haje Korth, James A. Slavin, Michael E. Purucker, and Sean C. Solomon. 2012. "Observations of Mercury's Northern Cusp Region with MESSENGER's Magnetometer." *Geophysical Research Letters* 39 (8). https://doi.org/10.1029/2012GL051472.